

# MD and multifrequency EPR studies of the dynamics of the MTSL spin-label in the activation loop of Aurora-A kinase protein

Maria Grazia Concilio,<sup>a,1\*</sup> Alistair J. Fielding,<sup>a,2\*</sup> Richard Bayliss,<sup>b,c</sup> and Selena G. Burgess<sup>b,c</sup>

<sup>a</sup>*The Photon Science Institute and School of Chemistry, EPSRC National EPR Facility and Service, University of Manchester, Manchester, M13 9PY, United Kingdom.*

<sup>b</sup>*Department of Molecular and Cell Biology, Henry Wellcome Building, University of Leicester, Leicester, LE1 9HN, United Kingdom.*

<sup>c</sup>*Cancer Research UK Leicester Centre.*

## Abstract

Classical molecular dynamics (MD) simulations, within the AMBER program package that runs entirely on a CUDA-enabled NVIDIA graphic processing unit (GPU), were employed to study the dynamics of the methane-thiosulfonate spin labelled (MTSL) Aurora-A kinase activation loop in a very short time and with good quality of the sampling. The MD simulation provided a wealth of information on the interactions between MTSL and protein residues, and on the different motional contributions to the overall dynamics of the MTSL that were validated using a multifrequency electron paramagnetic resonance (EPR) approach. The latter relied on the frequency dependence of the resolution of the fast and slow motions of the spin probe and was used to distinguish the fast internal motion of the spin label from the slow protein tumbling. Data obtained from MD were in good agreement with those obtained from quantum mechanical (QM) methods, but more interactions within the dynamics of the system were revealed than from QM. A strong correlation between the tumbling of the protein and the transitions of the  $\chi_4$  dihedral angle of the MTSL was observed with a consequent effect on the distribution of the nitroxide (NO) group in space and time. The theoretical EPR spectra were calculated using selected configurations of MTSL probing different micro-environments of the protein characterized by different polarity. The comparison between the theoretical and experimental 9 GHz and 94 GHz EPR spectra revealed that some fits were in good agreement with the experimental EPR spectra, indicating a predominance of some conformational states of the full spin-labelled system. This work is a starting point for deeper experimental and theoretical studies of the diffusion properties of the Aurora-A kinase protein related to its overall tumbling and biological activity.

---

<sup>1\*</sup> First corresponding email address: [mariagrazia.concilio@postgrad.manchester.ac.uk](mailto:mariagrazia.concilio@postgrad.manchester.ac.uk)

<sup>2\*</sup> Second corresponding email address: [alistair.fielding@manchester.ac.uk](mailto:alistair.fielding@manchester.ac.uk)

## 1. Introduction

Electron paramagnetic resonance (EPR) spectroscopy combined with site directed spin labelling (SDSL) is a technique widely employed to investigate structural properties and dynamical processes of biological systems.<sup>1-2</sup> This has provided valuable information on many proteins such as T4 lysozyme,<sup>3</sup> lipoxygenase L-1,<sup>4</sup>  $\alpha$ -synuclein,<sup>5</sup> bacteriorhodopsin,<sup>6</sup> SNARE<sup>7</sup> and NavMs.<sup>8</sup> Studies on singly labelled proteins can reveal a wealth of information on the tumbling and diffusion properties of the target. In addition data of the tumbling of protein can be gained by analysis of the continuous-wave (CW) EPR lineshape.<sup>9-10</sup> A common spin label employed to study structural and dynamic properties of biomolecules by EPR spectroscopy is MTSL.<sup>11</sup> The relationship between EPR lineshape and the underlying protein dynamics is not without ambiguities due to the large number of variables that can affect the EPR magnetic parameters ( $g$ - and  $A$ -tensors) and processes that produce nitroxide reorientation in the protein environment.

In order to provide a realistic interpretation of the CW EPR spectrum of spin labelled systems, a description of the dynamics of the MTSL spin label in the protein environment and the effect of protein tumbling on the spin label has to be found. Several different computational approaches to determine the conformational space and dynamics of the MTSL spin label and subsequently simulate the EPR spectrum have been recently suggested. Some approaches are based on Brownian Dynamics (BD) and molecular dynamics (MD) methods<sup>12-13</sup> to generate stochastic dynamical trajectories of the spin label in the full protein environment.

Brownian trajectories can be obtained using two simple models introduced by Robinson and co-workers<sup>14</sup> and is based on a two states jumps (TSJ) model that describes spin hopping between two positions in a lattice and the isotropic rotational Brownian diffusion (IRD) model that describes the isotropic rotation of the molecule in which trajectories are generated by a discretized form of the Fokker-Plank (FP) diffusion equation. In these two approaches the stochastic evolution of the system in time is based on kinetic Monte

Carlo algorithms or more recent quaternion-based Monte Carlo algorithms.<sup>15</sup> Another approach based on the Brownian Dynamics method was developed by Steinhoff and co-workers<sup>16</sup> and employs the Langevin equation to generate Brownian Dynamics (BD) trajectories from which Larmor frequencies and magnetization trajectories are subsequently calculated. The EPR spectrum is then obtained from the Fourier-Laplace transform of the magnetization trajectories. Stochastic dynamical trajectories can also be obtained using MD simulations with accurate parameterization of the force fields, appropriate water models and consideration of the decay of the re-orientational auto-correlation function of the spin labelled system.<sup>12-13</sup> Another approach was developed by Budil and co-workers<sup>17</sup> and utilises diffusion operator-based stochastic Liouville equation formalism to calculate the slow-motional EPR spectrum. In this approach MD trajectories are generated to derive diffusion parameters such as the rotational diffusion tensors, diffusion tilt angles and expansion coefficients of the orienting potentials that are then incorporated in the stochastic Liouville equation (SLE) calculation. Other methods include the Discrete-state stochastic Markov jump model from MD trajectories and temperature scaling or replica<sup>18-19</sup> exchange methods including simulated tempering (ST), applied in the context of Markov chain Monte Carlo simulations<sup>20</sup>, and parallel tempering (PT) that have been developed to improve sampling and kinetic information. However the force field is not parametrized to capture energetics of the interactions. Approaches to simulate the EPR spectra directly from BD or MD are based on a single truncated dynamical trajectory generated to the point at which the correlation function of rotational dynamic of the MTSL is completely relaxed.<sup>21-22</sup> There are also integrated computational approaches (ICA) that link a quantum mechanical (QM) method rooted on density functional theory (DFT) to the stochastic Liouville equation SLE-equation in the FP form. A similar approach was used to calculate the CW EPR spectra of free radicals in their environments<sup>23-25</sup> and to study the structure and dynamics of the MTSL side chain in protein systems, such as T4 lysozyme.<sup>26-27</sup> The models produced were in good

agreement with experimental data with a reasonable computational cost<sup>28-30</sup> and consistent with data obtained by MD simulations.<sup>31-32</sup> In these approaches QM methods were used to determine EPR parameters (*g*- and *A*-tensors) and used coarse grained methods to produce a hydrodynamic model of the diffusion tensor<sup>33</sup> that are the input of the SLE equation for the calculation of the CW EPR spectra.<sup>25,34</sup> There are also computationally inexpensive approaches that can be used to predict the distribution of the conformations of the spin labels and distances between spin-labelled sites, such as MMM,<sup>35</sup> PRONOX<sup>36</sup> and MtsslWizard<sup>37</sup>.

In this work, we used a MD/QM approach to investigate the relationship between the solution state CW EPR lineshape and the dynamics of the spin labelled activation loop of Aurora-A kinase. We introduced MTSL into the activation loop of Aurora-A kinase at residue 288. To allow this modification, the wild-type threonine residue was mutated to cysteine. Aurora-A kinase is a Serine/Threonine protein kinase that regulates mitotic entry, centrosome maturation and bipolar spindle assembly and is overexpressed in a number of cancers including breast, colorectal, ovarian, and glioma.<sup>38-39</sup> Kinase activity is tightly regulated by conformational changes in a conserved region of the protein known as the activation loop upon phosphorylation and binding of the activator protein Targeting Protein for Xklp2 (TPX2).<sup>40-41</sup> The conformation of the activation loop may also be influenced by the binding of inhibitors to the active site of Aurora-A and, in the case of the potent and selective inhibitor MLN8054, the position of the activation loop main chain is moved by up to 19 Å.<sup>42</sup> The understanding of kinase structure is mostly based on protein crystallography, which is limited by the requirement to trap the molecules within a crystal lattice.<sup>43-45</sup> Therefore, studies of kinase activation, through characterisation of activation loop conformations in solution, are important to enhance the understanding of molecular processes related to diseases and to support the discovery of small molecule kinase inhibitors.

In this work, MD simulations of opportune length were performed to determine how MTSL occupies space around the point of attachment in the loop and to provide insight on

the coupling between the motions of the MTSL spin label and the tumbling of the protein. The quality of the sampling was assessed by comparing the configurations determined from MD with structures determined at the minima of the torsional energy profiles of the dihedral angles of the MTSL calculated with a QM method based on DFT. Comparisons between the root mean square deviations (RMSD) of the loop and of the MTSL and the evolution of the dihedral angles of the MTSL were made to identify the correlations between their dynamics. Analysis of the auto-correlation function was used to determine the different motional contributions to the overall dynamics of the MTSL. Subsequently, a number of configurations were chosen from MD in different environments of the protein and used for calculation of the relevant EPR parameters (*g*- and *A*-tensors) and then the 9 GHz and 94 GHz CW EPR spectra of the spin-labelled Aurora-A kinase.

## 2. Methods

### 2.1 Force field parameterization of the MTSL side chain

The latest AMBER force field<sup>46</sup> (ff14SB), recommended for the study of protein dynamics was extended in order to perform MD calculations with AMBER 2015.<sup>47</sup> The structure of the MTSL side chain was first optimized with the B3LYP hybrid functional using the 6-31G(d) basis set. This level of theory was used as it provided accurate experimental geometries of the MTSL spin label<sup>31</sup> in previous work. Subsequently, in order to reproduce the electrostatic potential and hydrogen-bonding properties of the MTSL side chain, the atom-centred point charges were calculated with HF/6-31G(d) as the level of theory using Gaussian09 revision d.01.<sup>48</sup> as it is the most appropriate to interface with AMBER 2015. The electrostatic potential was calculated using the restrained electrostatic potential (RESP) procedure<sup>49</sup>. The atom charges used to extend the AMBER force field to the MTSL side chain were comparable with those reported in literature.<sup>28</sup>

## 2.2 MD simulation

MD simulations were carried out on MTSL spin labelled Aurora-A kinase, using the X-ray crystal structure of the Aurora-A kinase domain (residues 122-403 C290A C393A; PDB 4CEG<sup>50</sup> with a resolution of 2.10 Å and R-value of 0.202) and the AMBER 15 package in conjunction with ff14SB protein force field. The pdb file was edited in the website WHATIF<sup>51</sup> to mutate the native Threonine-288 to cysteine. The missing crystallographic hydrogens and MTSL were added using the LEaP module AMBER. The protein was solvated using the Extended Simple Point Charge (SPC/E) water model (9721 water molecules) in a truncated octahedral box with a buffer of 12 Å between the protein atoms and the edge of the box. This water model was used as it predicts viscosities and diffusion constants closer to the experimentally observed data<sup>52</sup> and reproduces crystallographic water positions more accurately than the commonly used Transferable Intermolecular Potential 3 Point (TIP3P) water model.<sup>13,52-53</sup> The MD simulation was performed in three main steps, minimization, equilibration and production. Firstly, a short energy minimization was performed in two steps in order to clean the structure and to remove bad contacts using the Simulated Annealing with NMR-derived Energy Restraints (SANDER) module of AMBER. Three chloride ions were used to neutralize the net charge. In the first stage, the water molecules and counter ions were relaxed with 200 cycles of minimization. In the second step, the entire system as a whole was relaxed with 1000 cycles of minimization. Subsequently, the system was heated at constant volume for 20 ps from 10 K to 300 K with 10 kcal/mol weak restraints on the protein. This process was followed by two equilibration steps, the first was performed at constant pressure (1 atm) and temperature (300 K) for 200 ps with no restraints and the second was performed in a microcanonical (NVE) ensemble for 1 ns. The production step was performed in the NVE ensemble for over 40 ns (in two steps of 20 ns + 20 ns) since transitions between rotamers occur on a time scale of ns and to ensure the auto-correlation function of rotational dynamic of the MTSL side

chain was completely relaxed.<sup>12-13,53-55</sup> All the calculations were performed using 1 fs integration time step and trajectory snapshots were collected every 2 ps. The NVE ensemble was used since the interest of this work is on the dynamics of a system that would be perturbed by the use of a thermostat. This system is large enough (with 14000 atoms in total) that microcanonical and canonical ensemble are almost the same.<sup>52</sup> The dynamical long-range electrostatic interactions were treated using a Particle mesh Ewald (PME) algorithm with default parameters and a 10 Å cut-off Lennard-Jones.

## 2.3 QM calculations

A small unit peptide was extracted from the structure of the Aurora-A kinase activation loop obtained after the full process of equilibration. Figure 1 shows the structure of the MTSL spin labelled Aurora-A kinase and the unit peptide extracted (black circle).

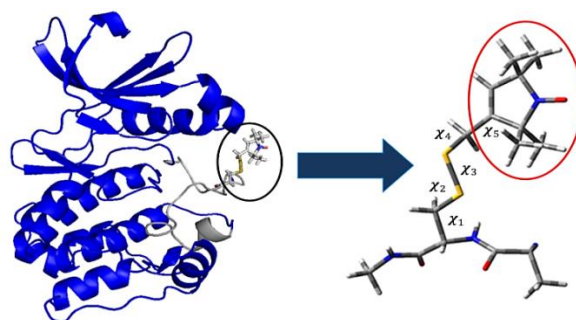


**Figure 1:** Structure of the Aurora-A kinase domain with the MTSL side chain (black circle) attached at position 288 within the activation loop which comprises residues 274 to 299 (grey). The unit peptide extracted for the DFT analysis is indicated by a blue arrow. All five dihedral angles of the MTSL side chain are enlarged and shown, with the pyrroline ring containing the nitroxide group highlighted in a red circle.

In order to provide reliable reproductions of the equilibrium geometries of the rotamers, the energy torsional profiles  $V_i(\chi_i)$  were calculated by performing relaxed scans in thirty-seven steps of 10° with the B3LYP hybrid functional<sup>56-57</sup> and the 6-31G(d) basis set<sup>58</sup> in gas phase around each dihedral angle ( $\chi_1$ ,  $\chi_2$ ,  $\chi_3$ ,  $\chi_4$  and  $\chi_5$ ) of the MTSL side chain using the unit peptide shown in Figure 1. The same model system was used in previous work.<sup>26,31,59</sup> The *ab initio* relaxed scans were performed using the `opt = modredundant` keyword in Gaussian 09 that fixes coordinates but optimises or relaxes the other atoms.

These scans helped to identify the minima of the torsional energy profiles of all five dihedral angles.

#### 2.4 Calculation of EPR parameters (*g*- and *A*-tensors)

The EPR parameters were calculated using the Gauge-Independent Atomic Orbital (GIAO)<sup>60</sup> method, the B3LYP hybrid functional and the latest N07D basis set that has been used with success for accurate calculation of the magnetic tensors ( $\Delta g_{ii} = \pm 0.0005$ ,  $\Delta A_{ii} = \pm 1$  G) in gas phase and in solution of nitroxide radicals at a reasonable computational cost<sup>12, 29, 61-62</sup> and can be downloaded from the DREAMSLAB website<sup>63</sup>. The Polarizable Continuum Model (PCM) was used to describe solvation in water since the experimental EPR spectrum was measured in water<sup>64-65</sup>. All the EPR spectra were simulated using the open source *Spinach* software library.<sup>66</sup> The slow-motion regime EPR spectra were simulated using the “SLE” implementation<sup>67-68</sup> based on the SLE-equation in the FP form, developed by Kubo<sup>69</sup> in the 1960’s and then adapted for EPR simulations by Freed and co-workers<sup>70-73</sup> for the calculation of slow motion and rigid limit spectra.<sup>71-74</sup> The Fokker-Planck formalism in *Spinach* generated spatial rotations or rotational diffusion of the spin system (hence other conformations) from the starting Cartesian coordinates obtained from the selected frames. The fast-motion regime EPR spectra were simulated using the Bloch-Redfield-Wangsness relaxation theory.<sup>75-76</sup>

#### 2.5 Experimental section

The expression construct for Aurora-A 122-403 T287A, T288C, C290A, C393A was produced in earlier work for recombinant expression of the protein in *E. coli* with a N-terminal TEV cleavable His<sub>6</sub>-tag.<sup>41</sup> Expression and purification of the kinase was carried out as previously stated with the following modifications.<sup>50</sup> After TEV cleavage and affinity chromatography to remove the His<sub>6</sub>-tag and His<sub>6</sub>-tagged TEV, 5 mM DTT was added to Aurora-A containing fractions and left to incubate overnight at 4 °C to ensure C288 was in the reduced form to allow subsequent

modification with MTSL. The reducing agent was removed by desalting of the protein on a HiPrep 26/10 Desalting column as per the manufacturer’s instructions (GE Healthcare) into 20 mM Tris pH 7.0, 0.2 M NaCl, 5 mM MgCl<sub>2</sub> & 10 % (v/v) glycerol (EPR buffer). 10-fold excess MTSL was added to the kinase and incubated overnight at 4 °C in order to spin label the kinase. Any remaining impurities, aggregated protein and excess MTSL were removed by size-exclusion chromatography using a HiLoad 16/600 Superdex 200 pg column as per the manufacturer’s instructions (GE Healthcare) into EPR buffer. SDS-PAGE analysis was used to identify fractions of high purity MTSL-Aurora-A 122-403 T287A, T288C, C290A, C393A which were concentrated and flash-frozen for future experiments. 50 μM MTSL-Aurora-A 122-403 T287A, T288C, C290A, C393A was used for CW EPR studies. 9 GHz measurements were performed using a Bruker Micro EMX spectrometer at 295 K, the modulation frequency was set at 100 KHz and the microwave power at 2.0 mW. The spin labelling efficiency was equal to 86% as measured following a published procedure.<sup>77</sup> 93.778 GHz CW measurements were performed on a Bruker E560 spectrometer. The magnetic field was calibrated using a Mn<sup>2+</sup> power standard (0.02% MgO) and the procedure described by O. Burghaus *et al.*<sup>78</sup> Dual-scan measurements were made in order to avoid hysteresis effects and a modulation frequency of 100 KHz and low microwave power (0.004800 mW) were used to avoid distortion of the lineshape.

### 3. Results and discussion

#### 3.1 Conformational analysis of the MTSL side chain from QM calculations

In order to provide reliable reproductions of the geometry of the rotamers, torsional energy profiles  $V^{(i)}(\chi_i)$  for all five of the dihedral angles of the MTSL side chain were computed using the subsystems shown in Figure 2.

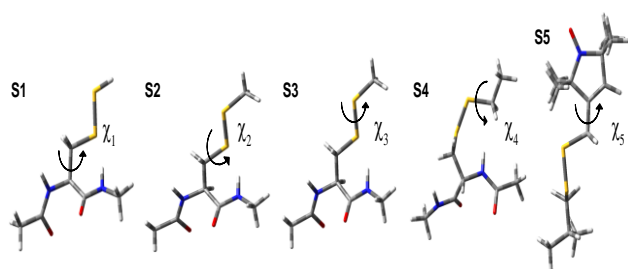


**Figure 2:** Subsystems considered for the calculations of the torsional energy profiles about the  $\chi_1$  (S1),  $\chi_2$  (S2),  $\chi_3$  (S3),  $\chi_4$  (S4) and  $\chi_5$  (S5) dihedral angles. The MTSL side chain was gradually built by adding atoms to the unit peptide.

The MTSL side chain was gradually built in by adding atoms to the  $C_\alpha$  atom of the  $\text{CH}_3\text{-CO-NH-C}_\alpha\text{-CO-NH-CH}_3$  fragment extracted from the minimized and equilibrated structure of the Aurora-A kinase domain in which the Cartesian coordinates of the peptide atoms were kept fixed in the configuration obtained after the previous scan. The relaxed scans were performed following the strategy shown in Figure 3. The energy minima of the  $\chi_{i+1}$  dihedral angle were determined at the minima of the  $\chi_i$  dihedral angle.

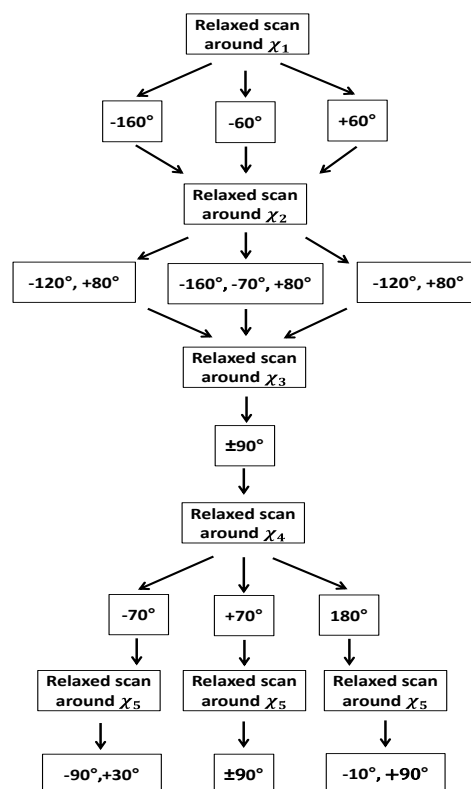


**Figure 3:** Strategy used to find minima of the torsional energy profile around  $\chi_1$ ,  $\chi_2$ ,  $\chi_3$ ,  $\chi_4$  and  $\chi_5$  dihedral angles from the relaxed scans. The first relaxed scan was performed around  $\chi_1$  and three minima at  $-160^\circ$ ,  $-60^\circ$  and  $+60^\circ$  were found. Subsequently the energy torsional profile was calculated around  $\chi_2$  at the minima of  $\chi_1$  and two minima, one broad between  $-160^\circ$  and  $-120^\circ$  and another at  $+80^\circ$  were found for  $\chi_1 = -160^\circ$  and  $+60^\circ$ . Three minima ( $-160^\circ$ ,  $-70^\circ$  and  $+80^\circ$ ) were found for  $\chi_1 = -60^\circ$ . The relaxed scan around  $\chi_3$  was performed at the minima of  $\chi_2$  and two minima  $\pm 90^\circ$  for all the possible combination of  $\chi_1$  and  $\chi_2$  were found. Three minima  $\pm 70^\circ$  and  $180^\circ$  were found in the torsional profiles of  $\chi_4$ . The torsional profile of  $\chi_5$  showed minima depending on the values of  $\chi_4$ .

The first torsional energy profile of the dihedral angle,  $\chi_1$  was obtained by performing relaxed scans in the range from  $-180^\circ$  to  $+180^\circ$ , considering the rotation of the  $C_\alpha\text{-C}_\beta\text{H}_2$  group attached to the  $\text{CH}_3\text{-CO-NH-C}_\alpha\text{H-CO-NH-CH}_3$  fragment. The torsional energy profile showed three minima at the values of  $-160^\circ$  and  $\pm 60^\circ$ . (Fig. 4A).

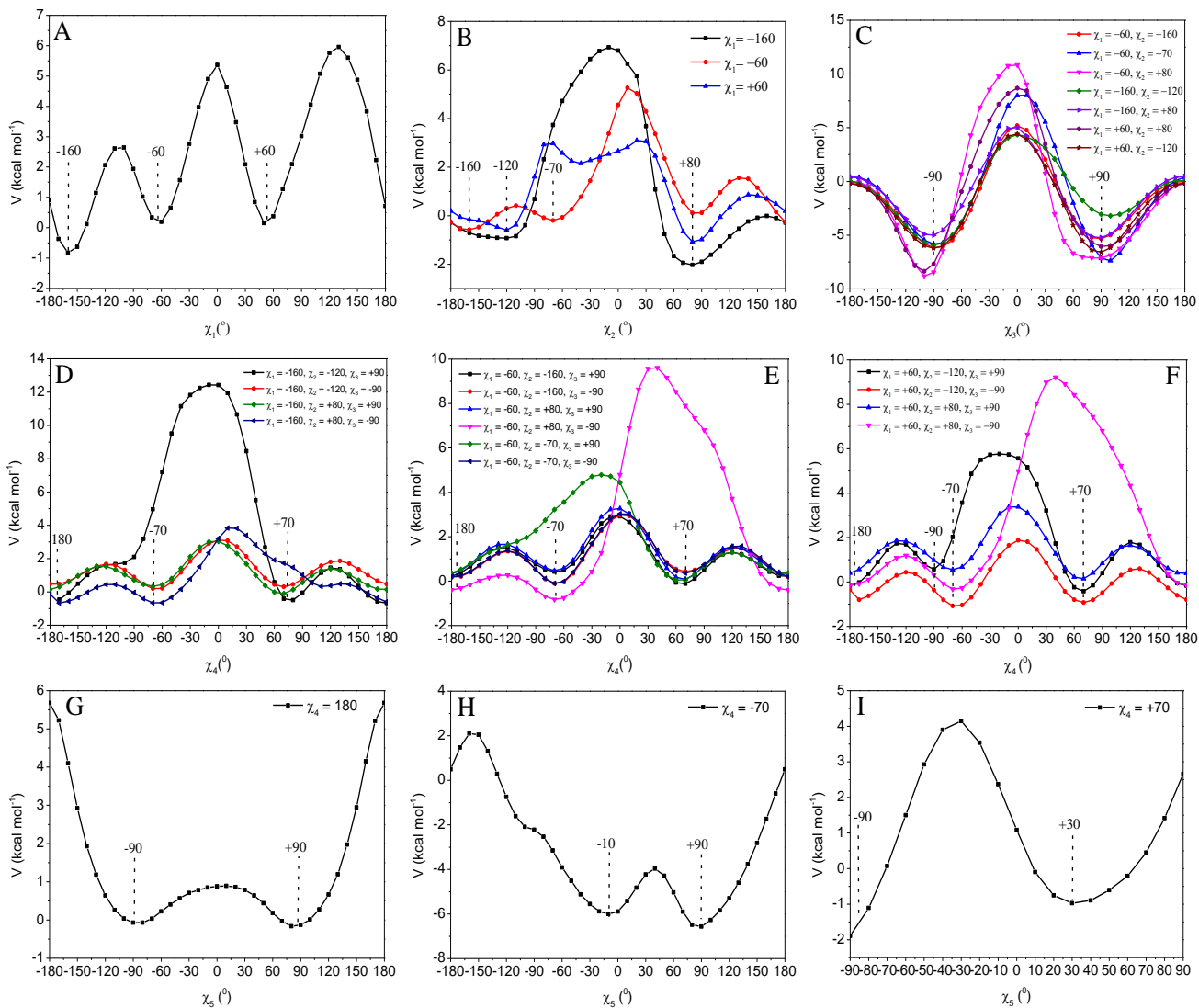


**Figure 4:** Energy torsional profiles about the five dihedral angles,  $\chi_1$ ,  $\chi_2$ ,  $\chi_3$ ,  $\chi_4$  and  $\chi_5$  of the MTSL side chain. (A) Energy torsional profile about the dihedral angle,  $\chi_1$ . (B) Energy torsional profiles about the dihedral angle,  $\chi_2$  at the minima of  $\chi_1$ . (C) Energy torsional profiles about the dihedral angle,  $\chi_3$  at the minima of  $\chi_2$ . (D-E-F) Energy torsional profile about the dihedral angle,  $\chi_4$  was calculated at the minima indicated in the insert. (G) Energy torsional profile about the dihedral angle,  $\chi_5$  when  $\chi_4$  is equal to  $180^\circ$ . (H) Energy torsional profile about the dihedral angle  $\chi_5$  when  $\chi_4$  is equal to  $-70^\circ$ . (I) Energy torsional profile about the dihedral angle  $\chi_5$  when  $\chi_4$  is equal to  $+70^\circ$ .

The high energy barriers corresponded to eclipsed configurations, while the lower energy barriers correlated to configurations in which the  $S_\gamma$  and  $S_\delta$  atoms were interacting with the protein backbone. The first torsional profile (Figure 4A),  $V^{(1)}(\chi_1)$  showed three broad minima and two transitions between  $-160^\circ \leftrightarrow -60^\circ$  and  $-60^\circ \leftrightarrow +60^\circ$  that were separated by an energy barrier of  $\sim 3$  kcal/mol and  $\sim 5$  kcal/mol, respectively. These energy barriers are somewhat small and transitions between them would be expected to

occur frequently. Subsequently, the  $V^{(2)}(\chi_2)$  torsional profiles were calculated considering the rotation around the  $C_\beta H_2-S_\gamma$  group attached to the  $C_\alpha$  atom of the  $CH_3-NH-CO-C_\alpha H-NH-CO-CH_3$  fragment. The  $\chi_1$  dihedral angle was set at  $-160^\circ$  and  $\pm 60^\circ$  (minima in the previous scan). In the calculated  $V^{(2)}(\chi_2)$  torsional profiles (Figure 4B) energy barriers of  $\sim 1-2$  kcal/mol between  $-120^\circ \leftrightarrow +80^\circ$  for  $\chi_1$  equal to  $-160^\circ$  and  $+60^\circ$ , and  $-160^\circ \leftrightarrow -70^\circ$  and  $-160^\circ \leftrightarrow +80^\circ$  for  $\chi_1$  equal to  $-60^\circ$  were observed. These transitions would be



expected to occur very frequently since they are separated by very small energy barriers, but are unlikely to do so considering the electrostatic interactions between the  $S_\gamma$  sulphur atom and the protein backbone. The torsional profiles about  $\chi_3$  were calculated at all these minima keeping the  $\chi_1$  and  $\chi_2$  dihedral angles fixed at the selected values shown in Figure 4C. For the calculation of the  $V^{(3)}(\chi_3)$  torsional profiles, the rotation around the  $C_\beta H_2 S_\gamma - S_\delta CH_2$  group attached to the  $C_\alpha$  atom of the  $CH_3 - NH - CO - C_\alpha H - NH - CO - CH_3$  fragment was considered. Similar energy torsional profiles and two minima at  $\pm 90^\circ$  separated by a higher energy barrier of  $\sim 14$  kcal/mol were found for  $V^{(3)}(\chi_3)$  for all seven possible combinations of the minima found for  $\chi_1$  and  $\chi_2$  (Figure 4C). The energy minima corresponded to the structures stabilized by short electrostatic interactions between atoms of the MTSL side chain and the unit peptide model as shown in Figure 5.

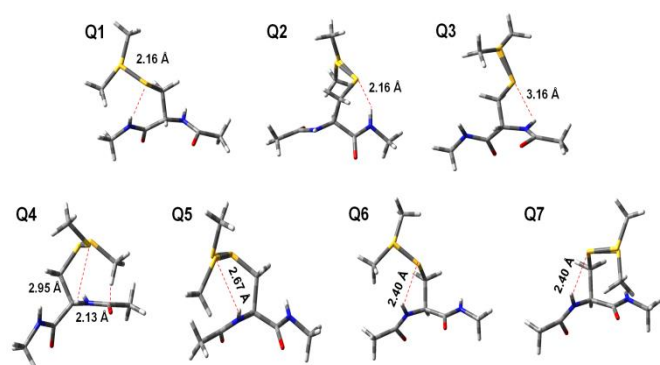


**Figure 5:** Interactions between atoms of the MTSL side chain and the unit peptide model for different values of  $\chi_1$ ,  $\chi_2$  and  $\chi_3$  (red dashed lines). Note that two conformations of  $\chi_3$  are shown in each panel. (Q1) Conformation at  $\chi_1 = -160^\circ$ ,  $\chi_2 = -120^\circ$  and  $\chi_3 = \pm 90^\circ$ . (Q2) Conformation at  $\chi_1 = -160^\circ$ ,  $\chi_2 = +80^\circ$  and  $\chi_3 = \pm 90^\circ$ . (Q3) Conformation at  $\chi_1 = -60^\circ$ ,  $\chi_2 = -160^\circ$  and  $\chi_3 = \pm 90^\circ$ . (Q4) Conformation at  $\chi_1 = -60^\circ$ ,  $\chi_2 = -70^\circ$  and  $\chi_3 = \pm 90^\circ$ . (Q5) Conformation at  $\chi_1 = -60^\circ$ ,  $\chi_2 = +80^\circ$  and  $\chi_3 = \pm 90^\circ$ . (Q6) Conformation at  $\chi_1 = +60^\circ$ ,  $\chi_2 = -120^\circ$  and  $\chi_3 = \pm 90^\circ$ . (Q7) Conformation at  $\chi_1 = +60^\circ$ ,  $\chi_2 = +80^\circ$  and  $\chi_3 = \pm 90^\circ$ .

The  $S_\gamma$  atom interacts with the NH group for  $\chi_1 = -160^\circ$  at  $\chi_2 = -120^\circ$  (Figure 5Q1),  $+80^\circ$  (Figure 5Q2) and for  $\chi_1 = -60^\circ$  at  $\chi_2 = -160^\circ$  (Figure 5Q3). The conformation at  $\chi_1 = -60^\circ$ ,  $\chi_2 = -70^\circ$  and  $\chi_3 = +90^\circ$  was stabilized by two short electrostatic interactions between the  $S_\delta$  atom of the MTSL chain and the  $C_\alpha H$  group in the fragment, and the  $CH_2$  group and the CO group (Figure 5Q4). The  $S_\delta$  atom interacts with the NH group

for  $\chi_1 = -60^\circ$  and  $\chi_2 = +80^\circ$  (Figure 5Q5). The conformation at  $\chi_1 = +60^\circ$ ,  $\chi_2 = -120^\circ$  and  $+80^\circ$  and  $\chi_3 = \pm 90^\circ$  (Figures 5Q6 and Q7) was stabilized by interactions between the  $S_\gamma$  atom of the MTSL and the NH group of the protein backbone. The remaining  $V^{(4)}(\chi_4)$  and  $V^{(5)}(\chi_5)$  torsional profiles (Figure 4D - I) were calculated considering the rotations around the  $S_\delta - CH_2$ -group (for  $\chi_4$ ) and  $S_\delta - CH_2$ -pyrroline nitroxide ring (for  $\chi_5$ ) with the previous dihedral angles kept fixed at the selected values. Like for  $V^{(3)}(\chi_3)$ , the  $V^{(4)}(\chi_4)$  torsional profiles (Figures 4D, E and F) were found to be independent from the values of the previous dihedral angles, probably due to the distance from the protein backbone. Similar torsional profiles for  $V^{(4)}(\chi_4)$  and three minima ( $\pm 70^\circ$  and  $180^\circ$ ) were observed for all possible combinations of  $\chi_1$ ,  $\chi_2$  and  $\chi_3$ . Two low energy barriers of 1-2 kcal/mol were found between the minima at  $\pm 70^\circ$  and  $180^\circ$  and the transitions  $180^\circ \leftrightarrow -70^\circ$  and  $180^\circ \leftrightarrow +70^\circ$  were considered, while a high energy barrier between  $-70^\circ$  and  $+70^\circ$  was found.

The  $V^{(5)}(\chi_5)$  torsional profile was measured at  $\pm 70^\circ$  and  $180^\circ$  and three different profiles were observed (Figure 4G, H and I). The  $V^{(5)}(\chi_5)$  profile at  $\chi_4 = +70^\circ$  was calculated between  $-90^\circ$  to  $+90^\circ$  due to a clash between one of the methyl groups of the pyrroline nitroxide ring and the  $C_\beta$  carbon of the MTSL chain for angles over this range. The shape of the torsional profiles obtained in this work is similar to those seen in  $\alpha$ -helices and values of the minima were found to be only slightly different,<sup>26,59</sup> indicating the protein backbone does not influence significantly the torsional profiles.

After calculation of the torsional energy profiles for all five dihedral angles in the unit peptide model, a population of 76 conformations was found at the minima of the torsional energy profiles. These conformations were then built into a larger region of the Aurora-A kinase protein activation loop obtained after the minimization and equilibration procedure. It was observed that 38 of the structures clashed with the protein backbone (*i.e.* when the distance between a pair of atoms is shorter than 75% of the sum of their van der Waals radii).<sup>26,31,79</sup> The torsional profiles showed low energy



barriers from 1 kcal/mol to ~20 kcal/mol and isoenergetic minima that indicate that the rotamer population would be fully sampled at room temperature and conformational states are expected to be obtained in the same amount.

### 3.2 Conformational dynamics of the MTSL spin label attached to activation loop of Aurora-A kinase using MD

Figure 6 shows plots of the occurrences of the dihedral angles during the course of the production step of the MD simulation (40 ns) on the full spin-labelled Aurora-A kinase protein that generated 40000 configurations.

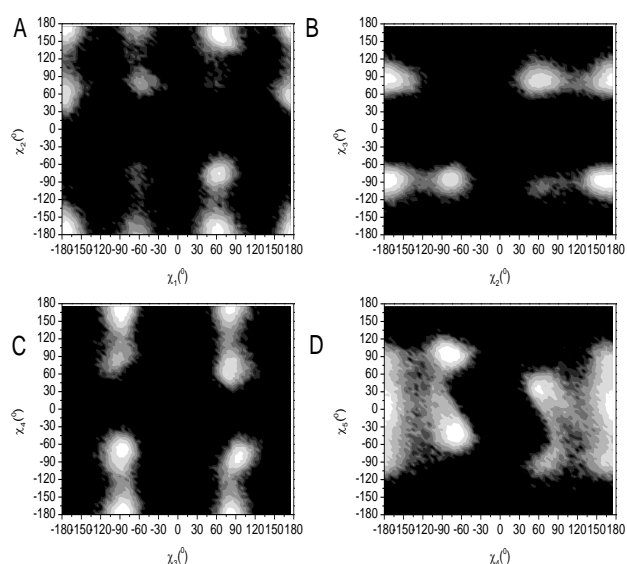


**Figure 6:** Plots of the occurrences of the  $\chi_i$ - $\chi_{i+1}$  dihedral angles, (A)  $\chi_1$ - $\chi_2$ , (B)  $\chi_2$ - $\chi_3$ , (C)  $\chi_3$ - $\chi_4$  and (D)  $\chi_4$ - $\chi_5$ . The most populated regions are white and the least populated regions are black.

A comparison of the torsional energy profiles (Figure 4) and the plots of the occurrences (Figure 6) revealed that the values of the minima determined by QM calculations were well reproduced by MD simulations. Three minima were found in the torsional profile of  $\chi_1$  corresponding to  $-160^\circ$ ,  $-60^\circ$  and  $+60^\circ$  (Figure 4 A) and the same three minima were found in the potential energy surfaces (Figure 6 A) from which the minima of  $\chi_2$  were confirmed and so on for  $\chi_3$ ,  $\chi_4$  and  $\chi_5$ . One difference found on comparison of the torsional profiles and the potential energy surfaces was that the minima  $\pm 60^\circ$  of  $\chi_1$  that are isoenergetic in the torsional profile have

a different energy in the  $\chi_1$ - $\chi_2$  potential energy surface. The energy of  $-60^\circ$  is much higher indicating that conformations with  $\chi_1 = -60^\circ$  are not favourable states in the full protein environments, probably due clashes with the protein backbone. If the free energy is estimated from the bin populations using  $G_i = -k_B T \ln \left( \frac{N_i}{N_{max}} \right)$ , where  $k_B$  is the Boltzmann's constant,  $T$  is the temperature,  $N_i$  is the population of the bin  $i$  and  $N_{max}$  is the population of the most populated bin, plots similar to those shown in Figure 6 were observed and the difference between high and low energy regions is  $\sim 2.82$  kcal/mol. This confirms what the rotamer population is expected to be fully sampled at room temperature which is in accordance with the results observed from QM calculations.

In order to identify a correlation between the evolution of the dihedral angles of the MTSL over time in relation to the activation loop motions, a comparison between the RMSDs to the starting structure of the MTSL (on residue 288) and the activation loop (residues 274 to 299) was carried out. In Figure 8 it is possible to distinguish four oscillation regions characterized by different amplitudes in the RMSDs of the activation loop and MTSL. During the MD simulation the activation loop oscillated between two extremes separated by 8 Å in which the MTSL was seen interacting with the  $\alpha$ -helix in front of the activation loop (Figure 8B green MTSL structure) in one frame and in two other frames interacting with both the tyrosine 208 and glutamine 209 (Figure 7B pink MTSL structure) and with tyrosine 208 only (Figure 7B blue MTSL structure). These conformational states are consistent with published crystal structures.<sup>40-41, 51</sup> The region probed by the pink and blue coloured MTSL labels in Figure 8B was not probed by rotamers determined at the minima of the torsional energy profiles and was subsequently not superimposed on the starting structure of the MD simulation, indicating that the dynamics of the protein is relevant for an appropriate sampling.

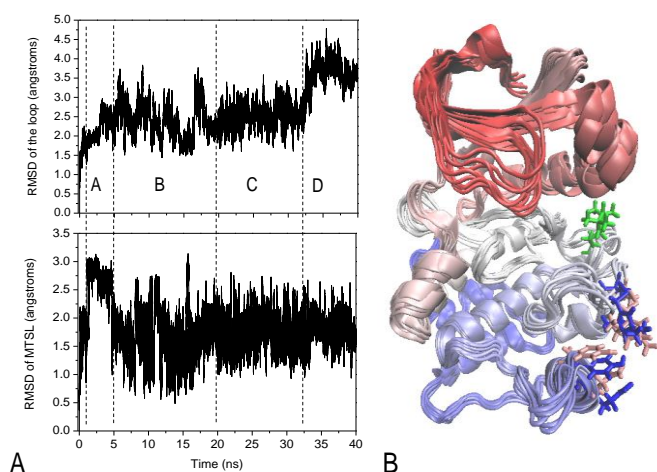


**Figure 7:** RMSD and MD analysis of the MTSL-labelled Aurora-A. (A) RMSDs of the activation loop and MTSL compared to the starting structure (considering atoms CA, C, N, O) from 0 - 40 ns. The black dotted vertical bars indicate different amplitude regions in which motions of the activation loop and the MTSL appear to be correlated. (B) Structures (10 frames) of the MTSL spin-labelled Aurora-A kinase protein extracted from the MD simulation showing the MTSL probing two regions over 16 Å.

The RMSD of the activation loop and MTSL were constant between 1 and 5 ns (Figure 7, region A). During this time the loop slowly oscillated between the two conformational states as shown in Figure 7B (region probed by the green and blue MTSL). Fast oscillations in the RMSD of the activation loop and MTSL were observed between 5 and 20 ns (Figure 7, region B) and moderate oscillations were observed from 20 to 32 ns (Figure 7, region C) corresponding to fast and moderate oscillations between the two conformational states. Moderate oscillations were observed from 32 ns to 40 ns (Figure 7, region D), in this region the RMSD of the loop changed from 2.5 Å to 3.7 Å, while the RMSD of the MTSL remained constant. The RMSD of the activation loop and of the MTSL were subsequently compared with the evolution of the dihedral angle of the MTSL (Figure 8).

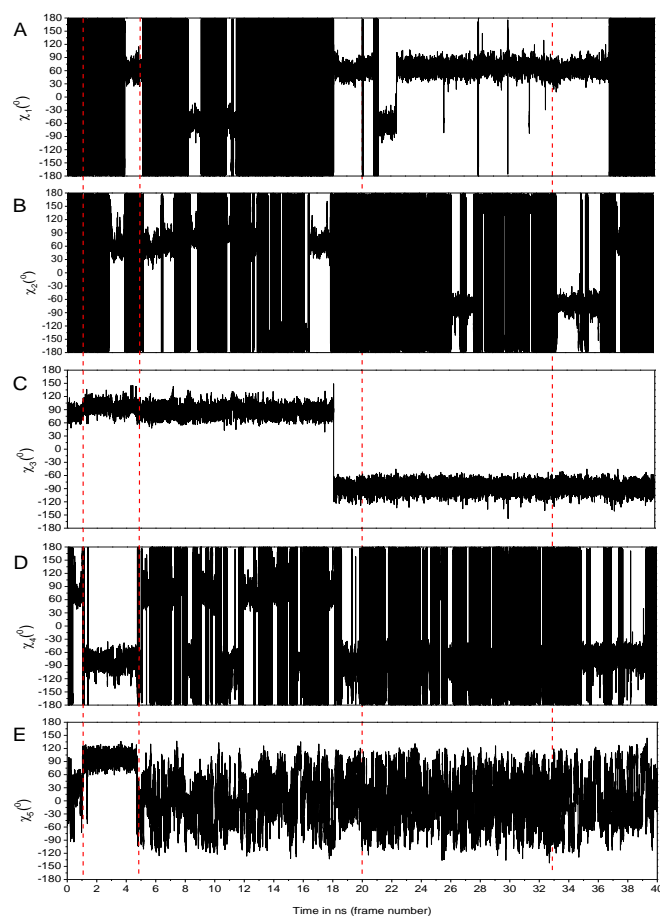


**Figure 8:** Plots showing the transitions of the  $\chi_1$  (A),  $\chi_2$  (B),  $\chi_3$  (C),  $\chi_4$  (D) and  $\chi_5$  (E) dihedral angles over 40 ns. The dotted red lines indicate the four regions A, B, C and D showed in Figure 7A.

As expected, slower transitions of  $\chi_1$ ,  $\chi_2$  and  $\chi_3$  were observed since they are separated by higher energy barriers, while  $\chi_4$  and  $\chi_5$  undergo rapid transitions due to the low energy barriers separating the conformational minima.

As observed in previous work, transitions often appear to be coupled. For example; the transition between  $\chi_4$  and  $\chi_5$  from 1 ns to 5 ns and the transition that simultaneously occurred around all five dihedral angles from 18 ns to 20 ns. Figure 8 shows transitions of  $\chi_1$  between  $-160^\circ \leftrightarrow +50^\circ$  and  $-160^\circ \leftrightarrow -60^\circ$  were observed frequently during the first 20 ns, while after 20 ns  $\chi_1$  was largely at  $+60^\circ$ . The transition of  $\chi_2$  between  $-160^\circ \leftrightarrow +80^\circ$  was slower in the range 0-18 ns and 26-38 ns and faster in the range 18-26 ns and 28-33 ns, respectively. The transition between  $\pm 90^\circ$  around  $\chi_3$  occurred just once over 40 ns due to the high energy barrier. Transitions of  $\chi_4$  and of  $\chi_5$  were quite slow for the first 5 ns then it became very fast for the remaining period of the

simulation. The RMSD of the activation loop and MTSL appear to be correlated to the evolution of the dihedral angles  $\chi_4$  and  $\chi_5$ . Values for  $\chi_4$  and  $\chi_5$  (Figure 8) and the RMSDs (Figure 7 region A) were constant from 1 to 5 ns. Transitions of  $\chi_4$  around  $+70^\circ \leftrightarrow 180^\circ \leftrightarrow -70^\circ$  were faster between 20 and 33 ns (Figure 8), where the oscillations of the RMSD were moderate, than in the region between 5 to 20 ns where the transitions were slower, while the oscillations of the RMSD are faster. Transitions of  $\chi_4$  were seen to be quite slow in the region from 33 to 40 ns, where oscillations of the RMSD were moderate after a change in the RMSD of the activation loop. This can be explained considering that fast oscillations of the loop slow down the rotations around the  $\chi_4$  dihedral angle. Almost all of the conformations determined at the minima of the torsional profiles were reproduced by the MD simulations. It was found that some conformations of the MTSL were seen to clash with the protein backbone in the profiles and did not in the MD simulation and instead probed different regions around the point of attachment of the label. This can be explained on consideration of the overall dynamics of the protein, which can change position and alter distances between atoms. Hence, in order to determine the conformational space probed by the MTSL it is necessary to consider the dynamics of the full system.

### 3.3 Comparison between CPU and GPU hardware in carrying out QM and MD calculations

A clear advantage of MD over QM methods is the time required to perform calculations. Table 1 shows speeds and the total time required for running all the torsional profiles shown in Figure 4 and the MD simulation.

**Table 1:** Timings used to run the QM calculations for the torsional profiles using the subsystems showed in Figure 2 and MD simulations of the MTSL spin-labelled Aurora-A kinase protein (4377 atoms) in 9721 water molecules.

Hardware configuration	Speed (s/day)	Total time (h)
QM on PC Intel CORE i7-4770 3.40 GHz CPU	-	490 <sup>1*</sup>
MD on computer cluster with MPI using 6GHz 256 CORE CPUs	~0.07	428 <sup>2*</sup>
MD on 2 x NVIDIA Tesla K40 12Gb GPU's	~30.21	33 <sup>3*</sup>

1\* Total CPU time using subsystems of 24 to 41 atoms showed in Figure 2.  
 2\* Total CPU time used to run the minimization and equilibration steps of the MD simulation.  
 3\* Total GPU time used for the full (minimization, equilibration and production steps) MD simulation.

QM calculations were carried out on a commercial computer desktop, while MD simulations were performed on a computer cluster and on a computer with a GPU. The full set of torsional profiles of the MTSL on a short peptide was obtained in about 490 hours, while MD simulation was performed on the full spin-labelled system in water in a comparable amount of time. Due to the large number of atoms in the system, queue limits and memory available to users it was not possible to complete the production step of 40 ns on the computer cluster. On a GPU it was possible to complete the full MD simulation in only 33 hours excluding post processing routines that took an additional few hours. The AMBER software used in this work was optimized to run entirely on a CUDA enabled NVIDIA GPU using a mixed-precision SPDP (single precision, double precision) model that is comparable with the double precision model on a central processing unit (CPU).<sup>80</sup>

### 3.4 Comparison between the RMSDs and the distribution of the nitroxide group (NO) in the activation loop environment

A comparison between the RMSD of the activation loop and MTSL with the distribution of the nitroxide (NO) group

revealed correlations between the dynamics of the system and the distribution of the NO in the space. Figure 9 shows the

distribution of the NO group in the space related to zones A, B, C and D zones of the RMSD (Figure 7).

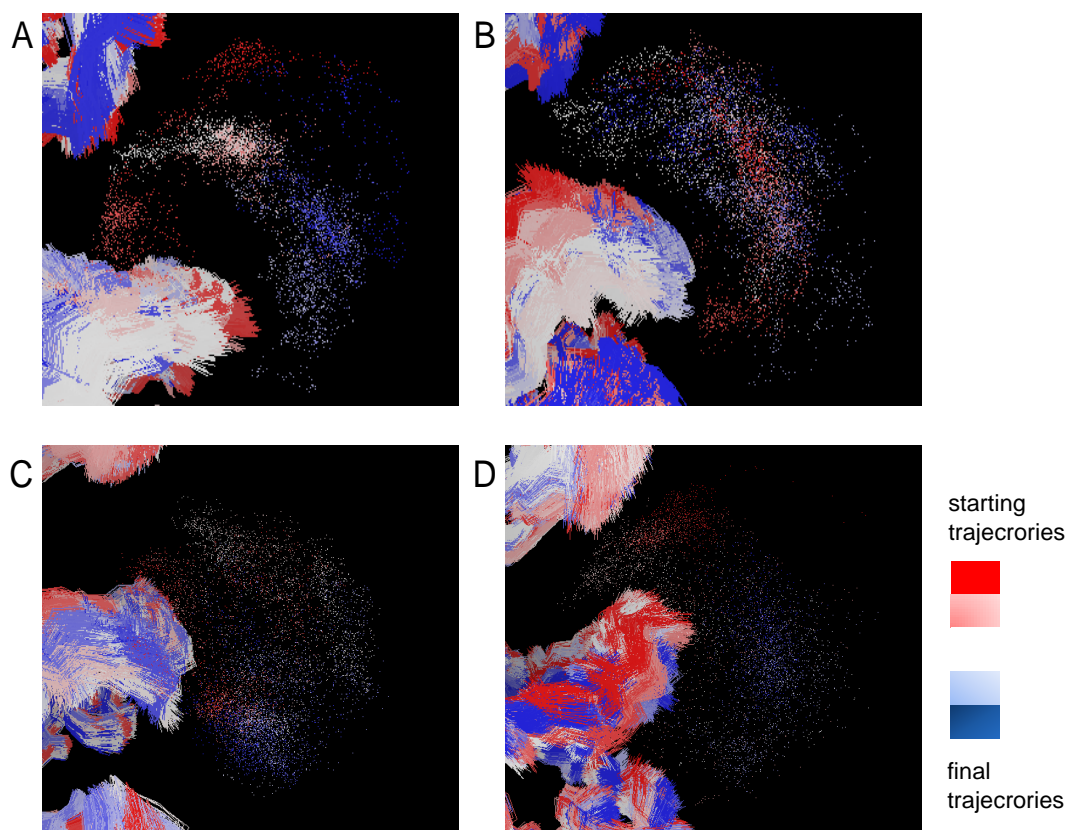


**Figure 9:** Snapshots from the MD simulation showing the distribution of the O atom of the MTSL NO nitroxide group in space. Trajectories collected from 1 to 5 ns (A), from 5 to 20 ns (B), from 20 to 32 ns (C) and from 32 to 40 ns (D). Red and blue points represent the initial and final trajectories in each snapshot, respectively. The colour evolution of the simulation is shown on the right.

Figure 9A shows the distribution of the NO group confined in five well-defined trajectory families generated by librational motion. This distribution corresponded to region A of Figure 7, where the RMSD of the activation loop and of the MTSL are quite constant and there are no transitions of the  $\chi_4$  and  $\chi_5$  (Figure 8). Figure 9B shows that the families of trajectories are well-distributed in the space where fast oscillations of the activation loop (Figure 7, region B) and fast transitions of  $\chi_4$  and  $\chi_5$  (Figure 8) were observed. Similarly in Figure 9C, corresponding to the region C of Figure 7, a wide distribution of trajectories in the space with a higher density of points in the region in which the MTSL interacts with a tyrosine residue was found. No trajectories between the activation loop and the  $\alpha$ -helix were found.

Figure 9D is a snapshot between 33 to 40 ns in which a jump in the RMSD of the activation loop from 2.5 Å to 3.7 Å and moderate oscillations of the RMSD were found and transitions of the  $\chi_4$  and  $\chi_5$  were quite slow leading to the presence of well-defined trajectory families.

Several important features arose from the MD simulation of Aurora-A kinase spin-labelled on the activation loop at residue 288. Looking at the snapshots in Figure 9, it is possible to observe that even for a short period of 5 ns the NO group is well distributed in the space around the point of attachment. During the course of the MD simulation, the MTSL was seen to be always exposed to the solvent water and free to diffuse in the space around the activation loop touching few groups of the protein.

Well-defined circular regions representing families of trajectories were observed when the activation loop was moving slowly (Figure 7A and D). In cases where the activation loop was moving faster the distribution of the NO group was very widespread in space all around the activation loop, as shown in Figure 9B and C. It was observed that the MTSL was randomly oriented in the space around the activation loop. The distribution of the MTSL seemed to strongly depend on the dynamics of the system and on the starting position of the trajectories.

### 3.5 Determination of the main motional contributions in the protein systems

The magnitude of the rotational correlation times,  $\tau_R$  of the internal motion of the MTSL was determined through analysis of the auto-correlation function of the dihedral angle  $\chi_4$ . The choice of using  $\chi_4$  is due to many X-ray crystallographic and spectroscopic studies of the rotameric states of the MTSL indicating that its internal dynamics arise predominantly from the dihedral angles  $\chi_4$ .<sup>55</sup> Furthermore, a correlation between the tumbling of the protein and the transitions of the  $\chi_4$  was observed in this work (Figure 8). Since transitions of  $\chi_4$  sometimes were sometimes seen to be faster and sometimes slower, a bi-exponential decay function was used to fit the auto-correlation function (Figure 10).

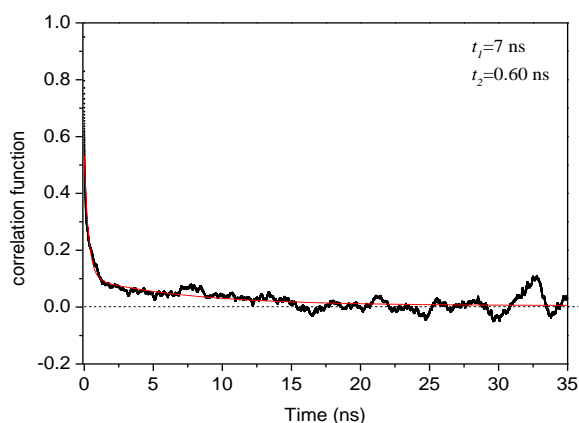


**Figure 10:** Auto-correlation function of the dihedral angle  $\chi_4$  (black line) and its fit (red line) using a bi-exponential function from which two correlation times were extracted, one equal to 7 ns and another of 0.60 ns.

Two correlation times were extracted using a bi-exponential fit, one equal to 0.60 ns and another equal to 7 ns, corresponding to slower and faster transitions of  $\chi_4$  ( $\pm 70^\circ$  and  $180^\circ$ ), in accordance to what was observed in Figure 8. The rotational correlation time of the tumbling of the protein is equal to 17 ns and was determined using the Stokes-Einstein-Debye equation  $\tau_R = \frac{k_B T}{8\pi\eta R_h^3} = \frac{1}{6D_r}$ , where  $k_B$  is the Boltzmann constant,  $T$  is the temperature,  $\eta$  is the viscosity of the water at 298 K,  $R_h$  is the hydrodynamic radius of the protein and  $D_r$  is the rotational diffusion coefficient.  $D_r$  was calculated for the PDB 4CEG structure of the Aurora-A kinase protein using the program HYDROPRO<sup>81</sup> and was equal to  $9.560 \times 10^6 \text{ s}^{-1}$ . Figure 11 shows a comparison between experimental and simulated 9 GHz and 94 GHz EPR spectra of the spin-labelled Aurora-A kinase protein, measured at 295 K, using the determined correlation times.

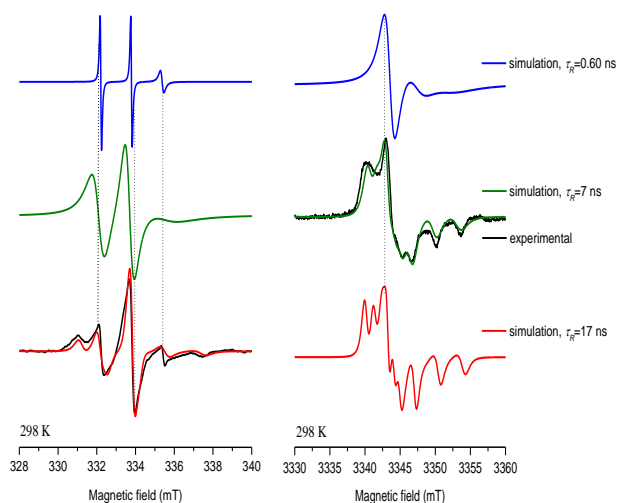


**Figure 11:** Comparison between experimental and simulated 9 GHz (on the left) and 94 GHz (on the right) EPR spectra using  $\tau_R = 0.60 \text{ ns}$ ,  $\tau_R = 7 \text{ ns}$  and  $\tau_R = 17 \text{ ns}$ .

It is possible to observe that simulations using  $\tau_R = 7 \text{ ns}$  and  $\tau_R = 0.60 \text{ ns}$  generated three sharp lines that did not fit the full spectrum at 9 GHz, while the simulation with  $\tau_R = 17 \text{ ns}$  fitted well to the full spectrum. At 94 GHz, a good fit was obtained using  $\tau_R = 7 \text{ ns}$ , while the simulations with  $\tau_R = 0.60 \text{ ns}$  and  $\tau_R = 17 \text{ ns}$  did not fit the full spectrum. The fits in Figure 10 were explained considering that at 9 GHz the slow motion related to the protein tumbling is

predominant while fast motions are averaged out. While at 94 GHz fast motions related the internal motion of the MTSL is predominant and the overall tumbling of the protein is not detected.<sup>82</sup>

### 3.6 Computation of $g$ - and $A$ -tensors and comparison between theoretical and experimental 9 GHz and 94 GHz CW EPR spectra of the spin-labelled Aurora-A kinase protein at position 288

During the course of the MD simulations the MTSL was seen to explore several regions around the activation loop and interact with several groups of the protein. The EPR spectra were simulated using five different configurations extracted from the MD simulation representing different micro-environments probed by the MTSL and characterized by different polarity (Figure 11).

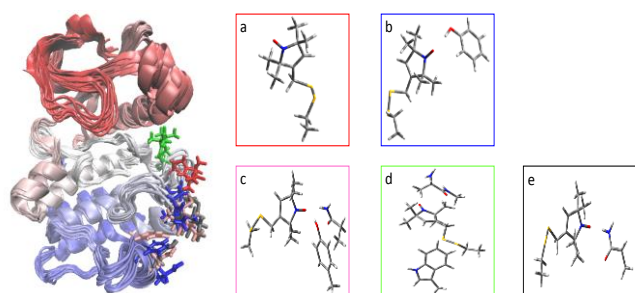


**Figure 11:** Five different frames extracted from the MD simulations showing the MTSL in different configurations represented by different colours. (a) The red MTSL is only exposed to the solvent water, (b) the blue MTSL is interacting with tyrosine 208, (c) the pink MTSL is interacting with the tyrosine 208 and glutamine 209 at the same time, (d) the grey MTSL is interacting with glutamine 209 and (e) the green MTSL is interacting with alanine 46 and tryptophan 151.

The 9 GHz and the 94 GHz EPR spectra of the spin-labelled Aurora-A kinase protein measured at 298 K and at 150 K, respectively, were simulated using the structures showed in Figure 11 and compared with the experimental data (Figure 12).

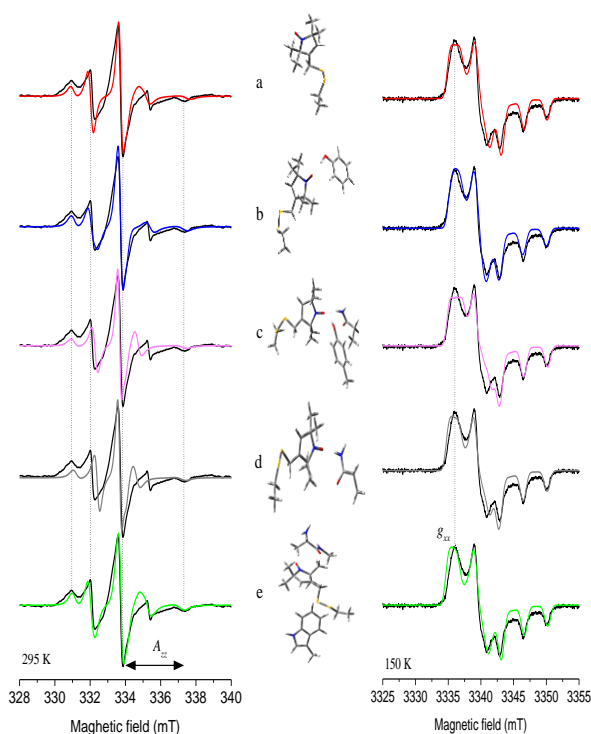


**Figure 12:** 9 GHz (left) and 94 GHz (right) EPR spectra measured at 298 K and 150 K, respectively. The black lines represent the experimental spectra and the coloured lines represent simulated EPR spectra using the structures showed in the insert corresponding to the structures shown Figure 11. The 9 GHz EPR spectrum was simulated using a correlation time of 17 ns. The horizontal arrow represents amplitude of the  $A_{zz}$  component of the hyperfine tensor and  $g_{xx}$  is the component of the  $g$ -tensor.

The simulated EPR spectra in Figure 12a, b and c reproduced experimental data quite well, especially b, while fits between spectra in Figure 12 c and d were in poor agreements. Similar spectra arose from other frames extracted from MD describing similar interactions. The spectra in Figure 12 c and d are characterized by smaller  $g_{yy}$  and  $A_{yy}$  and a bit slightly larger  $A_{xx}$  and is visible in both 9 GHz and the 94 GHz EPR spectra, especially at the 94 GHz. The EPR spectra in Figure a and e are characterized by larger  $A_{xx}$  and smaller  $A_{yy}$ , while the EPR spectrum b is characterized by reasonable  $A$ - and  $g$ -tensors. Figure 12 also shows also the effect of the polarity of the different micro-environments on the  $A_{zz}$  component of the hyperfine tensor and on the  $g_{xx}$  component of the  $g$ -tensor due to the electric field along the  $x$ - and  $z$ -axes of the nitroxide bond (NO).<sup>83</sup> 9 GHz EPR spectra are dominated by the hyperfine anisotropies and it is possible to determine the amplitude of  $A_{zz}$ , while the  $g$ -tensor is well-resolved at 94 GHz. Structures a, b and c in

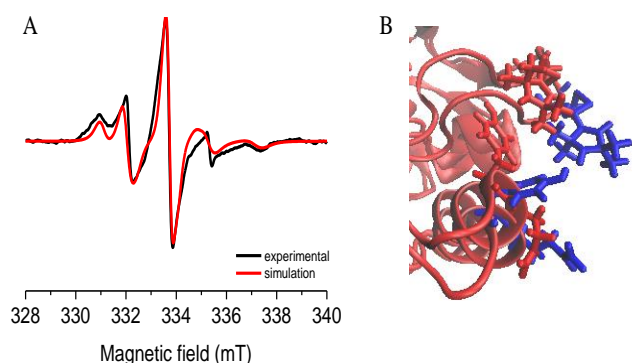


Figure 12 are located in polar environments, structure d is located in a less polar environment, while structure e is located in a nonpolar environment. Table 2 shows the evolution of the  $A_{zz}$  component and the  $g_{xx}$  components. The  $A_{zz}$  was seen increasing with the polarity of the environment (from e to a), while the  $g_{xx}$  was observed increase with decreasing polarity (from a to e).

**Table 2:** Evolution of the  $g_{xx}$  and  $A_{zz}$  with the polarity of the micro-environments.

Structure	$A_{zz}$ (mT)	$(g_{xx}-2)\times 10^4$
a	3.70	84
b	3.64	84
c	3.64	85
d	3.48	86
e	2.47	87

The full EPR spectrum of the Aurora-A kinase protein can be well-simulated using one correlation time of 15 ns, assuming an isotropic tumbling of the protein, and considering structures a, b and d that were seen to be the most favourable configurations adopted by the MTSL during the MD simulation (Figure 13A).



**Figure 13:** (A) Comparison experimental and simulated 9 GHz EPR spectra measured at 298 K obtained summing spectra a, b and e showed in Figure 12. (B) Two configurations showing the distance between the MTSL and tyrosine 208 and glutamine 209, respectively.

Both structures c and d showed an interaction between the MTSL and glutamine 209 that was seen to occur very rarely. Figure 13B shows different configurations, extracted at different times from the MD simulation, showing the MTSL

very close to the tyrosine (about 2.93 Å in the blue configuration and 3.43 Å in the red configuration) and very apart from the glutamine (about 7 Å in the blue configuration and 12 Å in the red configuration). This indicates that the distance between the two conformational states shown in Figure 7 does not go over 8 Å, preventing the MTSL interacting with the glutamine 209.

#### 4. Conclusion

The work performed here demonstrates advantages of running MD simulations on GPU compared to QM methods. A better description of the conformational space of the MTSL in the full protein environment was produced in a shorter timeframe. Conformational states of the MTSL obtained from MD simulations were in good agreement with those obtained from QM calculations with the advantage that the dynamics of the full system was considered and revealed interactions between the MTSL and residues of the protein not detectable on a “static” structure. The analysis of the RMSDs of the activation loop and MTSL revealed they are correlated with the evolution of the torsional profiles of the MTSL. It was observed that protein tumbling mainly affected the transitions of  $\chi_4$  and  $\chi_5$  and consequently the distribution of the nitroxide group (NO) in the space. During the course of the MD simulation, the MTSL was randomly oriented in the activation loop environment and the exchange between families of trajectories appeared to be dependent on the dynamics of the system and on the position of the starting trajectories. The micro-environments surrounding the label were seen to be characterized by different polarity and its effect on the NO group was investigated through the comparison between experimental and theoretical EPR spectra measured at 9 GHz and 94 GHz. The theoretical 9 GHz EPR spectrum measured at 298 K were well-simulated using just one correlation time of 17 ns, indicating isotropic tumbling of the protein. The internal motion of the MTSL was seen not to be very relevant at 9 GHz, but was fully detected at 94 GHz. The agreement between simulated and experimental EPR spectra was seen to be consistent with that

observed from the MD simulation that showed the MTSL diffusing in the water and located in polar and nonpolar regions. A realistic picture of the MTSL in the Aurora-A kinase protein was provided in a relatively simple way using publically available software without over parameterizations. This detailed protocol can be easily applied to other spin and/or biological systems to test a broad applicability.

## 5. Future works

The correlation between the tumbling of the protein and the evolution of the  $\chi_4$  with consequent effect on the NO distribution in the space revealed the necessity to develop more stochastic theoretical models to directly connect the tumbling of the protein with the conformational states of the label. This theoretical methodology has to provide a univocal, consistent and general way for the interpretation of the EPR spectra of biological systems attributing a physical meaning to parameters included in it and be easy to apply by a broader community without any over parameterization. In addition, longer MD simulations can be performed to study conformational changes of the activation loop on longer time scales and studies of the cross correlation between the RMSD and the evolution of the dihedral angles could be performed to improve understanding of the most stable structures in a larger ensemble.

## Author contribution

M. G. Concilio designed the full project described in this paper, ran all the EPR experiments, all the MD and DFT calculations, calculated all the theoretical EPR spectra and analysed the data. S. G. Burgess made the MTSL-spin labelled Aurora-A used for EPR spectroscopy. M. G. Concilio wrote the full paper with contributions from R. Bayliss, S. G. Burgess and A. J. Fielding.

## Acknowledgments

This work was supported by a studentship from Bruker Ltd. and a Cancer Research UK grant (C24461/A12772 to R.B). The authors would like to acknowledge the use of the EPSRC UK National Service for Computational Chemistry Software (NSCCS) and its staff (Dr. Alexandra Simperler and Dr. Helen Tsui for some technical advice) at Imperial College London in carrying out this work. This work is a result of many discussions within the EPR and computational communities. M. G. Concilio acknowledges NVIDIA for providing the Tesla K40 12Gb GPU machine used, Dr. A. Baldansuren and Prof. D. Collison for useful discussions EPR lineshape analysis; Dr. N. Burton, Prof. A. Polimeno and Dr. A. Simperler for useful feedback on the paper.

## Reference

1. M. Drescher and G. Jeschke, *EPR Spectroscopy: Application in Chemistry and Biology*, Springer, Berlin, pp. 237 (2012).
2. A. J. Hoff, *Advanced EPR: Applications in Biology and Biochemistry*, Elsevier, Amsterdam, pp. 918 (1989).
3. Z. Zhang, M. R. Fleissner, D. Tipikin, Z. Liang, J. K. Moscicki, K. Earle, W. Hubbell and J. H. Freed, *J. Phys. Chem. B* **114**, 5503 (2010).
4. B. J. Gaffney, M. Bradshaw, S. Frausto, J. H. Freed, and P. P. Borbat. *Biophysical J.* 103, 2134 (2012).
5. S. C. Drew, S. L. Leong, C. L. Pham, D. J. Tew, C. L. Masters, L. A. Miles, R. Cappai, K. J. Barnham, *J. Am. Chem. Soc.* **130**, 7766 (2008).
6. H. J. Steinhoff, *Biol. Chem.* **385**, 913 (2004).
7. D. Fasshauer, *Biochim. Biophys. Acta* **1641**, 87 (2003).
8. C. Bagn ris, P. G. Decaen, B. A. Hall, C. E. Naylor, D. E. Clapham, C. W. Kay and B. A. Wallace, *Nat. Commun.* **4**, 2465 (2013).
9. W. D. Toledo, V. V. Khramtsov, D. Cascio, C. Altenbach and W. L. Hubbel, *J. Magn. Reson.* **232**, 53 (2013).
10. W. L. Hubbell, H. S. Mchaourab, C. Altenbach and M. A. Lietzow, *Structure.* **4**, 779 (1996).
11. A. J. Fielding, M. G. Concilio, G. Heaven and M. A. Hollas, *Molecules.* **19**, 16998 (2014).
12. V. S. Oganessian, *Electron Paramag. Resonan.* **24**, 32 (2015).
13. G. Jeschke, *Prog. Nucl. Mag. Res. Sp.* **72**, 42 (2013).
14. B. H. Robinson, L. J. Slutsky, F. P. Auteri, *J. Chem. Phys.* **96**, 2609 (1992).

15. S. C. DeSensi, D. P. Rangel, A. H. Beth, T. P. Lybrand, E. J. Hustedt, *Biophys J.* **94**, 3798 (2008).
16. H. J. Steinhoff, W. L. Hubbell, *Biophys. J.* **71**, 2201 (1996).
17. D. E. Budil, K. L. Sale, K. A. Khairy, P. G. Fajer, *J. Phys. Chem. A.* **110**, 3703 (2006).
18. H. Li, M. Fajer, W. Yang, *J. Chem. Phys.* **126**, 024106 (2007).
19. M. I. Fajer, H. Li, W. Yang, P. G. Fajer, *J. Am. Chem. Soc.* **129**, 13840 (2007).
20. B. A. Berg, Markov Chain Monte Carlo Simulations and Their Statistical Analysis World Scientific, Singapore, (2004).
21. V. S. Oganessian, *J. Magn. Reson.* **188**, 196 (2007).
22. V. S. Oganessian, *Phys. Chem. Chem. Phys.* **13**, 4724 (2011).
23. V. Barone and A. Polimeno, *Phys. Chem. Chem. Phys.* **8**, 4609 (2006).
24. L. Hermosilla, C. Sieiro, P. Calle, M. Zerbetto and A. Polimeno, *J. Phys. Chem. B*, **112**, 11202 (2008).
25. M. Zerbetto, A. Polimeno, V. Barone, *Comput. Phys. Commun.* **180**, 2680 (2009).
26. F. Tombolato, A. Ferrarini and J. H. Freed, *J. Phys. Chem. B* **110**, 26248 (2006).
27. F. Tombolato, A. Ferrarini and J. H. Freed, *J. Phys. Chem. B* **110**, 26260 (2006).
28. E. Stendardo, A. Pedone, P. Cimino, M. C. Menziani, O. Crescenzi and V. Barone, *Phys. Chem. Chem. Phys.* **12**, 11697 (2010).
29. V. Barone, P. Cimino and E. Stendardo, *J. Chem. Theory Comput.* **4**, 751 (2008).
30. V. Barone, and P. Cimino, *Chem. Phys. Lett.* **454**, 139 (2008).
31. D. Sezer, J. H. Freed and B. Roux, *J. Phys. Chem. B* **112**, 5755 (2008).
32. D. Sezer, J.H. Freed, and B. Roux. *J. Phys. Chem. B* **112**, 11014 (2008).
33. V. Barone, M. Zerbetto, A. Polimeno, *J. Comput. Chem.* **30**, 2 (2009).
34. A. Polimeno, V. Barone, and J.H. Freed. Ed. Wiley: New York, NY, Chapter 12 (2012).
35. Y. Polyhach, E. Bordignon, G. Jeschke, *Phys. Chem. Chem. Phys.* **13**, 2356 (2010).
36. M. M. Hatmal, Y. Li, B. G. Hegde, P. B. Hegde, C.C. Jao, R. Langen, et al., *Biopolymers* **97**, 35 (2012).
37. G. Hagelueken, R. Ward, J. H. Naismith, O. Schiemann, *Appl. Magn. Reson.* **42**, 377 (2012).
38. A. R. Barr and F. Gergely, *J. Cell Sci.* **120**, 2987 (2007).
39. J. R. Bischoff, L. Anderson, Y. Zhu, K. Mossie, L. Ng, B. Souza, B. Schryver, P. Flanagan, F. Clairvoyant, C. Ginther, C. S. Chan, M. Novotny, D. J. Slamon and G. D. Plowman, *EMBO J.* **17**, 3052 (1998).
40. R. Bayliss, T. Sardon, I. Vernos, E. Conti, *Mol. Cell.* **12**, 851 (2003).
41. F. C. Rowan, M. Richards, R. A. Bibby, A. Thompson and R. Bayliss, J. Blagg, *ACS Chem. Biol.* **8**, 2184 (2013).
42. C. A. Dodson, M. Kosmopoulou, M.W. Richards, B. Atrash, V. Bavetsias, J. Blagg and R. Bayliss, *Biochem. J.* **427**, 19 (2010).
43. J. A. Endicott, M. E. Noble and L. N. Johnson, *Annu. Rev. Biochem.* **81**, 587 (2012).
44. M. Huse and J. Kuriyan, *Cell.* **109**, 275 (2002).
45. S. S. Taylor and A. P. Kornev, *Trends. Biochem. Sci.* **36**, 65 (2011).
46. J. A. Maier, C. Martinez, K. Kasavajhala, L. Wickstrom, K. E. Hauser, C. J. Chem. Theory Comput. **11**, 3696 (2015).
47. D. A. Case, J. T. Berryman, R. M. Betz, D. S. Cerutti, T. E. Cheatham, III, T. A. Darden, R. E. Duke, T. J. Giese, H. Gohlke, A. W. Goetz, N. Homeyer, S. Izadi, P. Janowski, J. Kaus, A. Kovalenko, T. S. Lee, S. LeGrand, P. Li, T. Luchko, R. Luo, B. Madej, K. M. Merz, G. Monard, P. Needham, H. Nguyen, H. T. Nguyen, I. Omelyan, A. Onufriev, D. R. Roe, A. Roitberg, R. Salomon-Ferrer, C. L. Simmerling, W. Smith, J. Swails, R. C. Walker, J. Wang, R. M. Wolf, X. Wu, D. M. York and P. A. Kollman (2015), AMBER 2015, University of California, San Francisco.
48. M. J. Frisch, G. W. Trucks, H. B. Schlegel, G. E. Scuseria, M. A. Robb, J. R. Cheeseman, G. Scalmani, V. Barone, B. Mennucci, G. A. Petersson, H. Nakatsuji, M. Caricato, X. Li, H. P. Hratchian, A. F. Izmaylov, J. Bloino, G. Zheng, J. L. Sonnenberg, M. Hada, M. Ehara, K. Toyota, R. Fukuda, J. Hasegawa, M. Ishida, T. Nakajima, Y. Honda, O. Kitao, H. Nakai, T. Vreven, J. A. Montgomery, Jr., J. E. Peralta, F. Ogliaro, M. Bearpark, J. J. Heyd, E. Brothers, K. N. Kudin, V. N. Staroverov, R. Kobayashi, J. Normand, K. Raghavachari, A. Rendell, J. C. Burant, S. S. Iyengar, J. Tomasi, M. Cossi, N. Rega, J. M. Millam, M. Klene, J. E. Knox, J. B. Cross, V. Bakken, C. Adamo, J. Jaramillo, R. Gomperts, R. E. Stratmann, O. Yazyev, A. J. Austin, R. Cammi, C. Pomelli, J. W. Ochterski, R. L. Martin, K. Morokuma, V. G. Zakrzewski, G. A. Voth, P. Salvador, J. J. Dannenberg, S. Dapprich, A. D. Daniels, Ö. Farkas, J. B. Foresman, J. V. Ortiz, J. Cioslowski, and D. J. Fox, Gaussian 09, Revision D.01, Gaussian, Inc., Wallingford CT, 2009.
49. C. I. Bayly, P. Cieplak, W. D. Cornell, P. A. Kollman *J. Phys. Chem.* **97**, 10269 (1993).
50. S. G. Burgess and R. Bayliss, *Acta Crystallogr. F. Struct. Biol. Commun.* **71**, 315 (2015).
51. G. Vriend, *J. Mol. Graph.* **8**, 52 (1990).
52. V. Wong, D. A. Case, *J. Phys. Chem. B* **112**, 6013 (2008).
53. P. Håkansson, P. O. Westlund, E. Lindahlb and O. Edholmb, *Phys. Chem. Chem. Phys.* **3**, 5311 (2001).
54. B. Roux, S. M. Islam. *J. Phys. Chem. B* **117**, 4733 (2013).
55. A. M. Popova, M. M. Hatmal, M. P. Frushicheva, E. A. Price, P. Z. Qin, I. S. Haworth. *J. Phys. Chem. B* **116**, 6387 (2012).

56. C. Lee, W. Yang and R.G. Parr, *Phys. Rev. B* **37**, 785 (1988).
57. A. D. Becke, *J. Chem. Phys.* **98**, 5648 (1993).
58. R. Ditchfield, W. J. Hehre and J. A. Pople, *J. Chem. Phys.* **54**, 724 (1971).
59. D. T. Warshaviak, L. Serbulea, K. N. Houk and W. L. Hubbell, *J. Phys. Chem. B* **115**, 397 (2011).
60. J. R. Cheeseman, G. W. Trucks, T. A. Keith and M. J. Frisch, *J. Chem. Phys.* **104**, 5497 (1996).
61. N. A. Chumakova, V. I. Pergushov, *Mendeleev Commun.* **24**, 301 (2014).
62. V. Barone, J. Bloino, M. Biczysko. *Phys. Chem. Chem. Phys.* **12**, 1092 (2010).
63. DREAMSLAB, accessed on 01 October, 2015, <http://dreamslab.sns.it/?pag=downloads>.
64. V. Barone, A. Bencini, M. Cossi, A. Di Matteo, M. Mattesini and F. Totti, *J. Am. Chem. Soc.* **120**, 7069 (1998).
65. L. Hermosilla, J. M. García de la Vega, C. Sieiro and P. Calle, *J. Chem. Theory Comput.* **7**, 169 (2011).
66. H. J. Hogben, M. Krzystyniak, G.T.P. Charnock, P.J. Hore, I. Kuprov, *J. Magn. Reson.* **208**, 179 (2011).
67. L. J. Edwards, D. V. Savostyanov, A. A. Nevzorov, M. Concistrè, G. Pileio, I. Kuprov, *J. Magn. Reson.* **235**, 121 (2013).
68. G. Moro and J. H. Freed, *J. Chem. Phys.* **74**, 3757 (1981).
69. R. Kubo, *J. Math. Phys.* **4**, 174 (1963).
70. A. Polimeno and H. J. Freed, *J. Phys. Chem.* **99**, 10995 (1995).
71. J. H. Freed, G. V. Bruno and C. F. Polnaszek, *J. Phys. Chem.* **75**, 3385 (1971).
72. L. J. Schwartz, A. E. Stillman and J. H. Freed, *J. Chem. Phys.* **77**, 5410 (1982).
73. A. A. Nevzorov and J. H. Freed, *J. Chem. Phys.* **112**, 1413 (2000).
74. R. P. Mason, J. H. Freed, *J. Phys. Chem.* **78**, 1321 (1974).
75. A. G. Redfield, *IBM J. RES. DEV.* **1**, 19 (1957).
76. R. K. Wangsness, and F. Bloch, *Phys. Rev.* **89**, 728 (1953).
77. M. Persson, J. R. Harbridge, P. Hammarström, R. Mitri, L. Mårtensson, U. Carlsson, G. R. Eaton, S. S. Eaton. *Biophys. J.* **80**, 2886 (2001).
78. O. Burghaus, M. Rohrer, T. Gotzinger, M. Plato and K. Mobius, *Meas. Sci. Technol.*, 1992, **3**, 765-774.
79. K. N. Beasley, B.T. Sutch, M. Hatmal, R. Langen, P. Z. Qin, S. I. Haworth, *Method Enzymol.*, **563**, 569 (2015).
80. A. W. Götz, M. J. Williamson, D. Xu, D. Poole, S. Le Grand and R. C. Walker. *J. Chem. Theory Comput.* **9**, 3878 (2013).
81. A. Ortega, D. Amoros, J. Garcia de la Torre, *Biophys. J.* **101**, 892 (2011).
82. Y. E. Nsmelov and D. D. Thomas, *Biophys Rev.* **2**, 91 (2010).
83. E. Bordignon, H. Brutlach, L. Urban, K. Hideg, A. Savitsky, A. Schnegg, P. Gast, M. Engelhard, E. J. Groenen, K. Möbius and Heinz-Juergen Steinhoff. *Appl. Magn. Reson.* **37**, 391 (2010).

